Check for updates

OPEN

Tunable resistivity of correlated VO$_2$(A) and VO$_2$(B) via tungsten doping

Songhee Choi[1], Gihyeon Ahn[2], Soon Jae Moon[2] & Shinbuhm Lee[1]✉

Applications of correlated vanadium dioxides VO$_2$(A) and VO$_2$(B) in electrical devices are limited due to the lack of effective methods for tuning their fundamental properties. We find that the resistivity of VO$_2$(A) and VO$_2$(B) is widely tunable by doping them with tungsten ions. When $x < 0.1$ in V$_{1-x}$W$_x$O$_2$(A), the resistivity decreases drastically by four orders of magnitude with increasing x, while that of V$_{1-x}$W$_x$O$_2$(B) shows the opposite behaviour. Using spectroscopic ellipsometry and X-ray photoemission spectroscopy, we propose that correlation effects are modulated by either chemical-strain-induced redistribution of V−V distances or electron-doping-induced band filling in V$_{1-x}$W$_x$O$_2$(A), while electron scattering induced by disorder plays a more dominant role in V$_{1-x}$W$_x$O$_2$(B). The tunable resistivity makes correlated VO$_2$(A) and VO$_2$(B) appealing for next-generation electronic devices.

Since the level of correlation effects between neighbouring electrons in the outermost $3d$ orbitals of vanadium ions differs depending on the crystal structure, the polymorphs of vanadium dioxide (VO$_2$) show a wide range of electrical properties, acting as an insulator in monoclinic VO$_2$(M1) and tetragonal VO$_2$(A), a semiconductor in monoclinic VO$_2$(B), and a conductor in tetragonal VO$_2$(R)[1–3]. Therefore, VO$_2$ polymorphs have been extensively studied for a range of interesting applications. VO$_2$(M1) and VO$_2$(R) have attracted wide interest for electronic devices since they show heat-, light-, electric field-, and chemical-induced reversible metal-insulator transitions near room temperature ($T_{MI} = 340$ K in bulk)[4–7]. On the other hand, VO$_2$(A) and VO$_2$(B) have been mainly used for energy applications, including redox-flow batteries, ion batteries, solid oxide fuel cells, hydrogen storage devices, and catalysts[8]. Compared to the many studies on electronic devices using VO$_2$(M1) and VO$_2$(R), however, the scarcity of published methods to tune the electrical properties of correlated VO$_2$(A) and VO$_2$(B) has limited their potential applications in electrical devices.

Several methods have been suggested for tailoring the correlation effects of VO$_2$(M1) since broad tunability of electrical properties is valuable for electrical devices. In addition to metallization induced by pressure application[9], hydrogen doping[10,11], or ionic liquid gating[12,13], cation doping has been widely used as a method with high efficacy. Chromium doping can result in transition of the dimerization of V−V chains in the VO$_2$(M1) phase into partial dimerization in the VO$_2$(M2) phase[14]. Substituting a small amount of tungsten for vanadium in VO$_2$(M1) causes notable changes in its electrical property[15]. For convenience, V$_{1-x}$W$_x$O$_2$ will be used herein to denote VO$_2$ with tungsten doping of $x \times 100\%$. As x increases, the resistivity of V$_{1-x}$W$_x$O$_2$ films decreases by several orders of magnitude, and T_{MI} also rapidly decreases at a rate of $dT_{MI}/dx = 2{,}100$–$2{,}800$ K. For $0.08 < x < 0.09$, the V$_{1-x}$W$_x$O$_2$ epitaxial films have a metallic ground state for a wide temperature range of 50–400 K. When x is increased beyond this range, V$_{1-x}$W$_x$O$_2$ reenters its insulating state.

Exploring tuning knobs of the electrical properties of VO$_2$(A) and VO$_2$(B) would not only enable their usage in electrical devices but also promote rich functionalities for energy devices. Motivated by research on correlated VO$_2$(M1), here, we investigate the effects of tungsten doping on the resistivity of correlated VO$_2$(A) and VO$_2$(B). We organize this paper as follows: first, we describe how, as the tungsten concentration increases, chemical strain increases the lattice parameters of both VO$_2$(A) and VO$_2$(B). Next, we find that tungsten doping is effective for tuning the resistivity of correlated VO$_2$(A) and VO$_2$(B) over a broad range. For $x < 0.1$–0.15, VO$_2$(A), an insulator in the pure phase, exhibits a monotonic decrease in resistivity of four orders of magnitude with increasing x. VO$_2$(B), a semiconductor in the pure phase, shows a monotonic increase in the resistivity of two orders of magnitude. Finally, to understand these opposite dependences, we explore the systematic evolution of the electronic

[1]Department of Emerging Materials Science, Daegu-Gyeongbuk Institute of Science and Technology, Daegu, 42988, Republic of Korea. [2]Department of Physics, Hanyang University, Seoul, 04763, Republic of Korea. ✉e-mail: lee. shinbuhm@dgist.ac.kr
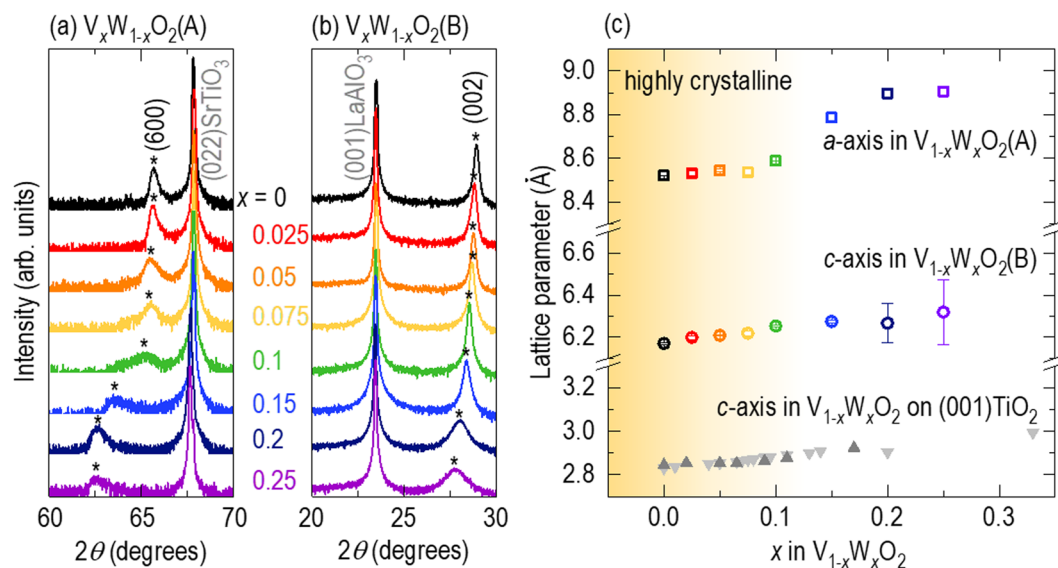
Figure 1. X-ray diffraction (XRD) θ–2θ scans for (**a**) $V_{1-x}W_xO_2(A)$ ($x \leq 0.25$) epitaxial films grown on (011)-oriented $SrTiO_3$ and (**b**) $V_{1-x}W_xO_2(B)$ epitaxial films grown on (001)-oriented $LaAlO_3$. The diffraction peaks of the films, highlighted by asterisks (*), are preserved for $x < x_c \approx 0.1$–0.15, but these intensities become weaker for $x > x_c$ due to film deterioration. With increasing tungsten concentration, $V_{1-x}W_xO_2(A)$ and $V_{1-x}W_xO_2(B)$ show a shift in their diffraction peaks towards lower 2θ values. (**c**) Tungsten concentration dependence of the lattice parameters of $V_{1-x}W_xO_2(A)$ and $V_{1-x}W_xO_2(B)$. We compare our results to the lattice parameters of $V_{1-x}W_xO_2$ epitaxial films grown on (001)-oriented TiO_2 (light grey[15] and grey[20] triangles). The lattice parameters show monotonic increases with increasing tungsten concentration. The region in graded yellow indicates preservation of the crystal structures when $x < x_c$.

structures and vanadium oxidation states by performing spectroscopic ellipsometry and X-ray photoemission spectroscopy (XPS), respectively.

Chemical tensile strain in $VO_2(A)$ and $VO_2(B)$ induced by tungsten doping.

Using pulsed laser epitaxy, we grew (100)-oriented $V_{1-x}W_xO_2(A)$ and (001)-oriented $V_{1-x}W_xO_2(B)$ epitaxial films on (011)$SrTiO_3$ and (001)$LaAlO_3$, respectively, for x from 0 to 0.25. We provided details of the deposition conditions in our previous reports[2,3,16–18] as well as in the Methods section. Figure 1a,b show the X-ray diffraction (XRD) $\theta - 2\theta$ scans of $V_{1-x}W_xO_2(A)$ and $V_{1-x}W_xO_2(B)$, respectively (see Fig. S1 for XRD $\theta - 2\theta$ scans in a wider 2θ range). We clearly observed (600)$VO_2(A)$ diffraction peaks for $x < 0.1$ and (002)$VO_2(B)$ diffraction peaks for $x < 0.15$, indicating preservation of the crystal structures for $x < x_c \approx 0.1$–0.15. However, for $x > x_c$, these XRD intensities significantly decreased, and some peaks disappeared, indicating that heavy doping of tungsten could lower the quality of our epitaxial $VO_2(A)$ and $VO_2(B)$ films [we ruled out possible effects of film thickness on the reduction of the XRD intensities since the X-ray reflectivity results (Fig. S2) revealed an almost invariant thickness of ~100 nm with tungsten doping.]. This observation is different from the seemingly preserved crystallinity up to $x = 0.33$ in $V_{1-x}W_xO_2$ epitaxial films grown on (001)-oriented TiO_2[15], which might be due to a strong strain effect between isostructural $VO_2(R)$ and TiO_2. Hereafter, we will mainly focus on the resistivity of $V_{1-x}W_xO_2$ ($x < x_c$) to avoid unwanted effects from film deterioration.

Substitution with tungsten ions, which are larger (0.60 Å)[19] than vanadium ions (0.58 Å), causes chemical tensile strain in $V_{1-x}W_xO_2(A)$ and $V_{1-x}W_xO_2(B)$ epitaxial films. As shown by the XRD $\theta - 2\theta$ scans, the (600)$VO_2(A)$ diffraction peak gradually shifts to a lower 2θ angle with increasing tungsten concentration (Fig. 1a), indicating an increase in the a-axis lattice parameter. We observe a similar behaviour for $V_{1-x}W_xO_2(B)$ films. The observation of the (002)$VO_2(B)$ diffraction peak at a lower 2θ angle with tungsten doping (Fig. 1b) indicates an increase in the c-axis lattice parameter. As shown in Fig. 1c, the a- and c-axis lattice parameters of $V_{1-x}W_xO_2(A)$ and $V_{1-x}W_xO_2(B)$ increase by 4.8% from 8.52 to 8.91 Å and by 2.4% from 6.17 to 6.32 Å, respectively, for $x = 0$–0.25. This chemical tensile strain is similar to the increase in the c-axis lattice parameter by 5.7% from 2.83 to 2.99Å for $x = 0$–0.33 in $V_{1-x}W_xO_2$ epitaxial films grown on (001) TiO_2 (for convenience of this calculation, we assumed that $V_{1-x}W_xO_2$ epitaxial films have a tetragonal structure on (001)TiO_2, although R, M1, and the intermediate phases could coexist in one film, as indicated by a broadened T_{MI})[15,20].

Tunable resistivity of $VO_2(A)$ and $VO_2(B)$ with tungsten doping.

With increasing tungsten concentration ($x < x_c$), the resistivity of $VO_2(A)$ decreased, while that of $VO_2(B)$ increased. Figure 2a shows the temperature dependence of the resistivity of $V_{1-x}W_xO_2(A)$ for $x = 0$–0.25. The resistivity of pure $VO_2(A)$ was very high, i.e., 4.37 Ω cm at 400 K, and increased with decreasing temperature. Such insulating behaviour is attributed to correlation-induced bandgap opening between unoccupied and occupied t_{2g} orbitals[1]. It should be noted that the resistivity of $V_{1-x}W_xO_2(A)$ decreased with x ($< x_c$, solid lines). The $V_{1-x}W_xO_2(A)$ epitaxial film for $x = 0.15$
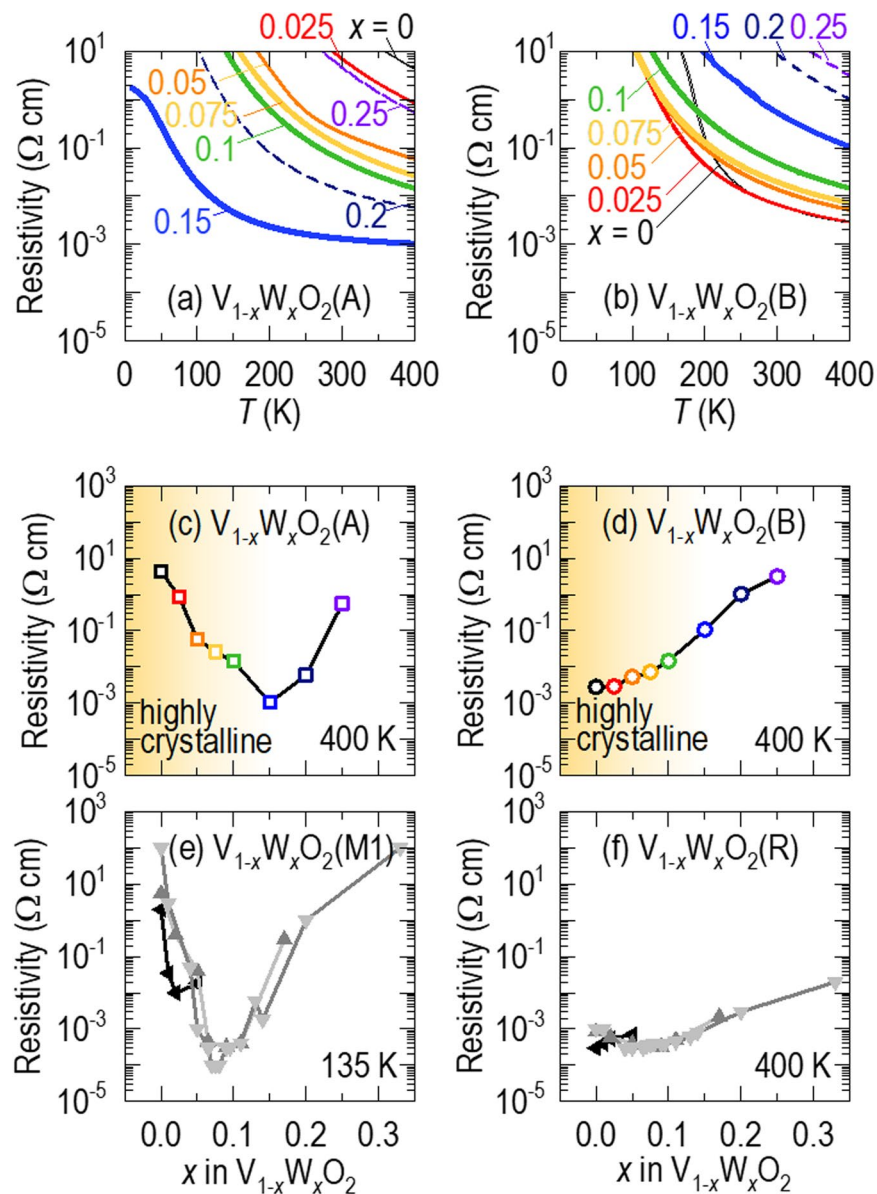
Figure 2. Tungsten concentration dependence of the resistivity-temperature curves of (**a**) $V_{1-x}W_xO_2$(A) and (**b**) $V_{1-x}W_xO_2$(B). The resistivity of the insulating VO_2(A) phase decreases as the tungsten concentration increases up to x_c (solid lines) but increases for $x > x_c$ (dashed lines). By contrast, the resistivity of the semimetallic VO_2(B) phase increases with increasing tungsten concentration for all x values. Comparison of the tungsten concentration dependences of the resistivity between (**c**) $V_{1-x}W_xO_2$(A) at 400 K, (**d**) $V_{1-x}W_xO_2$(B) at 400 K, (**e**) $V_{1-x}W_xO_2$(M1) at 135 K, and (**f**) $V_{1-x}W_xO_2$(R) at 400 K. We plotted data for $V_{1-x}W_xO_2$(M1) and $V_{1-x}W_xO_2$(R) from the literature (light grey[15], grey[20], and black[22] triangles). For $x < x_c$, the resistivities of insulating (A and M1) and metallic (B and R) materials decrease and increase, respectively. For $x > x_c$, the resistivities of all films increase. The region in graded yellow for $x < x_c$ indicates that the crystal structures are preserved.

showed a smaller resistivity (by three orders of magnitude) of 0.001 Ω cm at 400 K than that of pure VO_2(A). This small resistivity indicated that the film was on the verge of metallicity, in terms of the Mott-Ioffe-Regel limit[21] (i.e., the material is regarded as a metal when the resistivity is smaller than 0.001 Ω cm.). The resistivity of $V_{1-x}W_xO_2$(A) increased for $x > x_c$ (dashed lines), probably due to film deterioration. As shown in Fig. 2b, the resistivity of pure VO_2(B) also increased with decreasing temperature, indicating insulating behaviour. However, its resistivity was close to the Mott-Ioffe-Regel limit[21] at 400 K and significantly smaller (by three orders of magnitude) than that of pure VO_2(A). Such a low resistivity in pure VO_2(B) is ascribed to thermal electron jumping across the very narrow bandgap (<25 meV) near room temperature[1]. The resistivity of $V_{1-x}W_xO_2$(B) increased with increasing x by two orders of magnitude. Moreover, the resistivity increased more for $x > x_c$, as observed in $V_{1-x}W_xO_2$(A).

We noted interesting features of the tungsten doping effects on the resistivity of $V_{1-x}W_xO_2$(A) and $V_{1-x}W_xO_2$(B) ($x < x_c$). The dependences were opposite: the resistivity of $V_{1-x}W_xO_2$(A) decreased, i.e., 4.37 → 0.01 Ω cm at 400 K for $x = 0 \to 0.1$, while $V_{1-x}W_xO_2$(B) showed increasing resistivity, i.e., 0.003 → 0.01 Ω cm. It is surprising

that the resistivities of VO_2(A) and VO_2(B) changed to such an extent, although we doped a relatively small amount ($x < 0.1$) of tungsten ions. Therefore, our work indicates that tungsten doping is promising for tuning the resistivity of VO_2(A) and VO_2(B). This extensive tunability is expected to provide many opportunities to realize both electronic and energy devices using correlated VO_2(A) and VO_2(B).

To obtain more information about these opposing and large dependences, we compared the tungsten-doping dependences of the resistivity in $V_{1-x}W_xO_2$(A) and $V_{1-x}W_xO_2$(B) to those in previous reports on $V_{1-x}W_xO_2$(M1) and $V_{1-x}W_xO_2$(R). It was simple to evaluate the resistivities of our $V_{1-x}W_xO_2$(A) and $V_{1-x}W_xO_2$(B) epitaxial films since, across a wide temperature range, they do not show any phase transitions. However, when we plotted the resistivities of $V_{1-x}W_xO_2$(M1) and $V_{1-x}W_xO_2$(R), we had to pay attention to the different resistivities of the M1 and R phases due to the T_{MI} variation induced by the tungsten doping. Figure 2c–f show the 400 K resistivities of $V_{1-x}W_xO_2$(A) and $V_{1-x}W_xO_2$(B), the 135 K resistivity of $V_{1-x}W_xO_2$(M1)[15,20,22], and the 400 K resistivity of $V_{1-x}W_xO_2$(R)[15,20,22]. We note three features of the tungsten doping effect across the polymorphs. (1) For light doping ($x < x_c$), at which the crystal structures are well preserved (highlighted in yellow), the resistivities of insulating VO_2(A) and VO_2(M1) decrease by 3–4 orders of magnitude compared to those in the pure phases, while semiconducting VO_2(B) and metallic VO_2(R) exhibit increases in the resistivity by 1–2 orders of magnitude compared to those in the pure phases. (2) It is quite surprising that the resistivities of $V_{1-x}W_xO_2$(A) and $V_{1-x}W_xO_2$(M1) can be smaller than those of $V_{1-x}W_xO_2$(B) and $V_{1-x}W_xO_2$(R) when doped with certain amounts of tungsten (e.g., $x \approx x_c$ in this work). (3) For heavy doping ($x > x_c$), all phases show increased resistivity. We suggest that the increases seen in $V_{1-x}W_xO_2$(A) and $V_{1-x}W_xO_2$(B) can be attributed to deterioration of the films because we observed suppression of diffraction peaks in the $\theta - 2\theta$ XRD scans (Fig. 1a,b). The similar dependences between VO_2(A) and VO_2(M1) and between VO_2(B) and VO_2(R) suggest that the proposed mechanisms underlying the tungsten doping effects in VO_2(M1) and VO_2(R) may apply to VO_2(A) and VO_2(B), respectively.

Electronic structures of tungsten-doped VO_2(A) and VO_2(B).

To better understand the opposing dependences on tungsten doping, we investigated the electronic structures of $V_{1-x}W_xO_2$(A) and $V_{1-x}W_xO_2$(B) epitaxial films for various x values. Figure 3a shows the optical conductivity $\sigma_1(\omega)$ of $V_{1-x}W_xO_2$(A) ($x = 0, 0.05, 0.1$) as a function of photon energy. Pure VO_2(A) (first row) exhibited opening of a correlation-induced bandgap[1]. For $x = 0.05$ (second row), a spectral weight distinctly appeared near 0.8 eV. For $x = 0.1$ (third row), the bandgap might be narrower than 25 meV at room temperature (Figs. S3 and S4), so the electrons in the occupied t_{2g} orbital could thermally jump into the unoccupied t_{2g} orbitals even at room temperature, consistent with the low resistivity shown in Fig. 2a. To examine the variation in optical spectra with x in more detail, we evaluated $\sigma_1(\omega)$ using Lorentz oscillators, $\sigma_1(\omega) = \frac{e^2}{m^*}\frac{N_D\gamma_D}{\omega^2 + \gamma_D^2} + \frac{e^2}{m^*}\sum_j \frac{N_j\gamma_j\omega^2}{\left(\omega_j^2 - \omega^2\right)^2 + \gamma_j^2\omega^2}$, where m^*, γ_j, and ω_j are the effective mass, damping coefficient, and angular frequency of the jth resonance line, respectively[23]. The first and second terms in $\sigma_1(\omega)$ represent the metallic Drude response and interband transitions, respectively. The β-peak represents an interband transition from occupied t_{2g} to unoccupied t_{2g} orbitals and shifts to a lower photon energy with increasing x. Additionally, a new peak (asterisk) appeared near 0.8 eV, representing the creation of an in-gap state between the occupied t_{2g} and unoccupied t_{2g} orbitals. The spectroscopic findings are consistent with the decrease in resistivity in $V_{1-x}W_xO_2$(A). It should be noted that the spectroscopic results for $V_{1-x}W_xO_2$(A) are similar to observations for $V_{1-x}W_xO_2$(M1)[24]. Figure 3b shows proposed changes in the electronic structures of VO_2(A) with tungsten doping, i.e., a shift of the unoccupied t_{2g} orbital towards the Fermi level and the appearance of a new in-gap state just above the Fermi level.

Different from $V_{1-x}W_xO_2$(A), the electronic structure of $V_{1-x}W_xO_2$(B) did not show any obvious changes. Figure 3c shows the $\sigma_1(\omega)$ of $V_{1-x}W_xO_2$(B) ($x = 0, 0.05, 0.1$) as a function of photon energy. Pure VO_2(B) in the first row exhibited a non-negligible spectral weight near zero photon energy[1], consistent with its low resistivity near room temperature shown in Fig. 2b. With increasing tungsten concentration, the β-peak moved very slightly towards higher photon energy, and the Drude response (yellow line) was suppressed. Although such a blueshift is very weak, it is somewhat consistent with the more resistive $V_{1-x}W_xO_2$(B) with increasing x. Figure 3d shows a very weak change in the electronic structure of VO_2(B) with tungsten doping. Therefore, we suggest that the resistivity increase in $V_{1-x}W_xO_2$(B) is attributable to mechanisms other than any simple change in the electronic structure.

Mechanisms underlying the tunable resistivity of tungsten-doped VO_2(A) and VO_2(B).

Taking our experimental results together, we found that the resistivities of VO_2(A) and VO_2(M1) and those of VO_2(B) and VO_2(R) have similar dependences on tungsten doping. Numerous studies have attributed the stabilization of metallic $V_{1-x}W_xO_2$(M1) to correlation variations, with structural distortion of V−V dimers[24–26] and band filling by electron doping[27], as we will explain in detail in the following paragraphs. In this stage, we aimed to understand the behaviours of $V_{1-x}W_xO_2$(A) and $V_{1-x}W_xO_2$(B) ($x < x_c$) by adapting and modifying the mechanisms in $V_{1-x}W_xO_2$(M1) and $V_{1-x}W_xO_2$(R).

$V_{1-x}W_xO_2$(A) shows tunable properties due mainly to correlation effects being modulated by chemical-strain-induced redistribution of V−V distances. Goodenough noted that vanadium oxides are metallic when the distance between vanadium ions is less than 2.94 Å[28]. VO_2(M1) is insulating because correlated electrons are localized in V−V dimers, where the asymmetric distances of V−V atoms inside and between dimers are 2.65 and 3.12 Å, respectively. It is widely accepted that the transition from insulating VO_2(M1) to metallic VO_2(R) is accompanied by a symmetric redistribution of V−V chains, with an even distance of 2.88 Å. When vanadium ions are replaced with tungsten, the X-ray absorption fine structure indicates that the local structure around each tungsten atom is intrinsically symmetric, with a tetragonal-like structure. Therefore, the nearby V−V dimers in a VO_2(M1) lattice are rearranged to form rutile-like VO_2 nuclei[25,26]. In VO_2(A), vanadium ions along the c-axis have alternating distances of 3.25, 3.11, and 2.77 Å at room temperature (< 162 °C)[29]. Although the XRD results

4
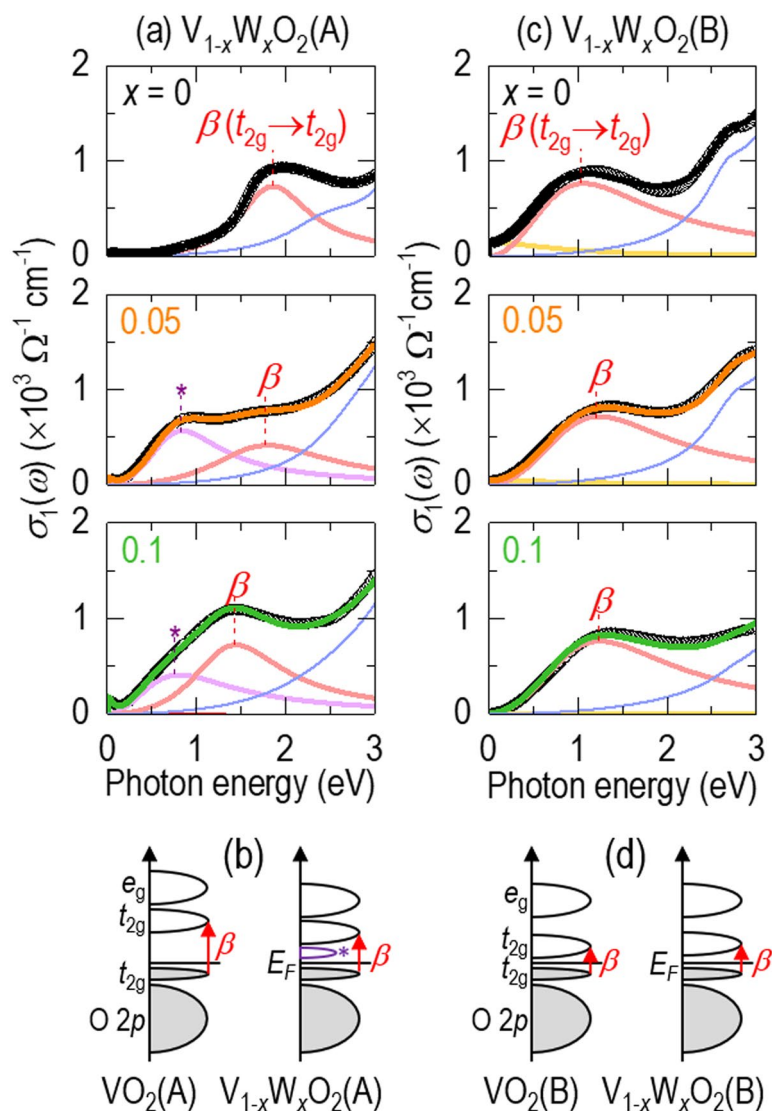
Figure 3. Evolution of the electronic structures of tungsten-doped $VO_2(A)$ and $VO_2(B)$. (**a**) Optical conductivity, $\sigma_1(\omega)$, of $V_{1-x}W_xO_2(A)$ ($x = 0, 0.05, 0.1$). Open circles represent experimentally measured $\sigma_1(\omega)$, and solid lines represent Lorentz oscillators. Due to optical transitions from occupied t_{2g} to unoccupied t_{2g} levels, the β-peak moves slightly towards lower photon energy for higher x. A new in-gap state (asterisk) appears near 0.8 eV. (**b**) Schematics of the electronic bandstructures of pure $VO_2(A)$ and $V_{1-x}W_xO_2(A)$. (**c**) $\sigma_1(\omega)$ of $V_{1-x}W_xO_2(B)$ ($x = 0, 0.05, 0.1$). For higher x, the β-peak moves slightly towards higher photon energy, and the Drude response (yellow line) is slightly suppressed. (**d**) Electronic bandstructure schematics of pure $VO_2(B)$ and $V_{1-x}W_xO_2(B)$.

imply that $V_{1-x}W_xO_2(A)$ mostly has a tetragonal structure similar to pure $VO_2(A)$, expansion of the local structure due to tungsten could symmetrize the V−V chains. This rearrangement would weaken the correlation effect in $V_{1-x}W_xO_2(A)$, leading to lower resistivity.

As an alternative mechanism for $V_{1-x}W_xO_2(A)$, we also considered electron doping since V^{4+} ions neighbouring the site of W^{6+} dopants change to V^{3+} ions to maintain charge neutrality[30]. This band filling drastically decreases the Coulomb repulsion energy and accordingly weakens the electron correlation[27], metallizing $V_{1-x}W_xO_2(M1)$. We also found a significant evolution of V^{3+} oxidation states in $V_{1-x}W_xO_2(A)$ with tungsten doping ($x = 0, 0.05, 0.1$). Figure 4 shows XPS V $2p_{3/2}$, V $2p_{1/2}$, and O $1s$ spectra in the binding energy range of 505–535 eV. We fitted the XPS spectra of pure $VO_2(A)$ (Fig. 4a) with $V^{4+}2p_{3/2}$ (red pattern) at 515.84 ± 0.2 eV and $V^{4+}2p_{1/2}$ (orange pattern) at $V^{4+}2p_{3/2} + 7.33$ eV[31], indicating that the oxidation state of our non-doped epitaxial films was firmly V^{4+}. Interestingly, V^{3+} peaks [$V^{3+}2p_{3/2}$ (blue pattern) at 515.29 ± 0.2 eV and $V^{3+}2p_{1/2}$ (purple pattern) at $V^{3+}2p_{3/2} + 7.33$ eV[31]] were additionally required to resolve the XPS spectra of $V_{1-x}W_xO_2(A)$ ($x = 0.05, 0.1$). It should be noted that the V^{3+} peaks were stronger with increasing x. This similar observation between $V_{1-x}W_xO_2(A)$ and $V_{1-x}W_xO_2(M1)$ indicates that electron-doping-induced band filling also plays an important role in tungsten-doped metallization[30].
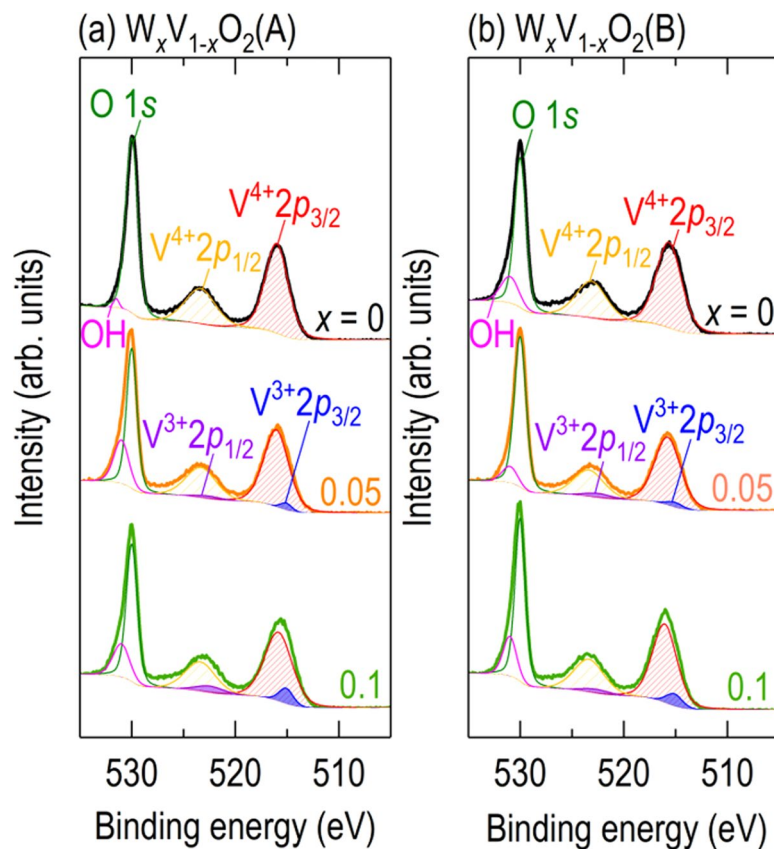
Figure 4. X-ray photoemission spectroscopy (XPS) V $2p_{3/2}$, V $2p_{1/2}$, and O $1s$ spectra of (**a**) $V_{1-x}W_xO_2$(A) and (**b**) $V_{1-x}W_xO_2$(B) in the binding energy range of 505–535 eV. While the XPS spectra of non-doped epitaxial films are fitted by V^{4+} peaks (red and yellow patterns), V^{3+} peaks (blue and purple patterns) are additionally required for the XPS spectra of $V_{1-x}W_xO_2$ ($x = 0.05, 0.1$). The intensity of the V^{3+} peaks increases with increasing x.

Although we also found significant evolution of the V^{3+} XPS peaks in $V_{1-x}W_xO_2$(B) (Fig. 4b), it is quite interesting to note that VO_2(B) became more insulating with increasing x. Therefore, we hypothesize that another mechanism, different from those for $V_{1-x}W_xO_2$(A) and $V_{1-x}W_xO_2$(M1), plays an important role in the tunable properties of $V_{1-x}W_xO_2$(B) ($x < x_c$). It should be noted that the correlation effects in VO_2(B) and VO_2(R) are weaker than those in VO_2(A) and VO_2(M1), considering their lower resistivities and narrower bandgaps[1,2]. Therefore, we suggest that the increase in resistivity in $V_{1-x}W_xO_2$(B) originates from disorder-induced electron scattering. Since more dopants will scatter more electrons, the resistivity will increase with heavier doping[32,33].

Conclusion

Tungsten doping provided an effective way to tune the resistivity of correlated VO_2(A) and VO_2(B). XRD revealed that the crystal structures of $V_{1-x}W_xO_2$(A) and $V_{1-x}W_xO_2$(B) expanded and were well preserved for $x < 0.1$–0.15. At this low doping concentration, the resistivity of $V_{1-x}W_xO_2$(A) decreased, similar to that of $V_{1-x}W_xO_2$(M1), with increasing tungsten concentration; in contrast, the resistivity of $V_{1-x}W_xO_2$(B) increased, similar to that of $V_{1-x}W_xO_2$(R). Spectroscopic ellipsometry revealed that tungsten doping resulted in a redshift of the unoccupied t_{2g} orbital, the creation of an in-gap state in $V_{1-x}W_xO_2$(A), and a slight blueshift of unoccupied t_{2g} orbitals in $V_{1-x}W_xO_2$(B). Both vanadate films showed evolution of the V^{3+} oxidation states based on the XPS study. Referring to the mechanisms in correlated $V_{1-x}W_xO_2$(M1), we proposed that $V_{1-x}W_xO_2$(A) and $V_{1-x}W_xO_2$(B) showed opposite dependences due to either chemical-strain-induced redistribution of V−V distances or electron-doping-induced band filling and disorder-induced electron scattering, respectively. We leave further consideration of the mechanisms for future studies.

The extreme tunability of correlated VO_2(A) and VO_2(B) enables their use in next-generation electronic devices, as well as energy devices. As we mentioned in the Introduction section, VO_2(M1) has shown a reversible resistivity change due to intercalation of hydrogen[10,11] and ionic liquid gating[12,13]. The similar doping dependence between VO_2(A) and VO_2(M1) suggests that these dynamic control methods would enable application of correlated VO_2(A) [also VO_2(B)] in memories, transistors, and gas sensors, as has been extensively studied for VO_2(M1).

Methods

Epitaxial film growth of tungsten-doped VO$_2$(A) and VO$_2$(B).   We recently optimized the growth conditions for epitaxial films of VO$_2$(A) and VO$_2$(B) on either perovskite oxides or Y-stabilized ZrO$_2$[2,3,16–18]. Using pulsed laser epitaxy, we deposited VO$_2$(A) and VO$_2$(B) epitaxial films on (011)-oriented SrTiO$_3$ and (001)-oriented LaAlO$_3$ substrates, respectively. We ablated a tungsten-doped V$_2$O$_5$ target with a KrF (248 nm wavelength) pulsed laser at a rate of 10 Hz and an intensity of 1 J cm^{-2}. For the targets, we mixed WO$_3$ and V$_2$O$_5$ powders in the desired molar ratio and sintered pellets at 650 °C for 12 hours in air. We used this low sintering temperature due to the low melting point (690 °C) of V$_2$O$_5$. We fixed the substrate temperature at 420 °C since VO$_2$(A) and VO$_2$(B) are thermodynamically unstable above 430 °C and transition into VO$_2$(R) above 470 °C[2,29]. We used a flow of oxygen gas with a partial pressure, P_{O_2}, of 8 mTorr for VO$_2$(A) and 15 mTorr for VO$_2$(B) since VO$_2$ stably forms in only a narrow range of 5 mTorr $< P_{O_2} <$ 30 mTorr[16,34].

Measurement of electrical and optical properties.   To investigate the electrical transport properties, we used a physical property measurement system (Quantum Design Inc.). We used the four-point probe method, which is the most common method for measuring the resistivity[35]. We deposited evenly spaced Pt contacts on the middle of the film surface. We applied a small constant current through the outer two contacts and measured the voltage between the inner two contacts. We swept the temperature in the range of 10–400 K. We measured the reflectance, $R(\omega)$, spectra in a photon energy range of 0.1–1 eV via a Fourier transform-type infrared spectrometer (model VERTEX 70 v; Bruker). We employed an *in situ* gold overcoating technique to obtain an accurate absolute value of $R(\omega)$. We obtained the optical conductivity of the VO$_2$ film via a two-layer model fit of the measured $R(\omega)$ with Drude-Lorentz oscillators[23,36]. We used spectroscopic ellipsometers (models V-VASE and M-2000; J. A. Woollam Co.) to obtain the complex dielectric constants, $\epsilon(\omega) = \epsilon_1(\omega) + i\epsilon_2(\omega)$, in the energy region between 1 and 5 eV. The optical conductivity, $\sigma_1(\omega)$, in this energy range can be calculated by $\sigma_1(\omega) = \epsilon_0\omega\epsilon_2(\omega)$[23], where ϵ_0 is the vacuum permittivity.

Characterization of structural properties and oxidation states.   We investigated the crystal structures via a four-circle high-resolution X-ray diffractometer (model Empyrean; PANalytical) using Cu radiation with a wavelength of 1.5406 Å. Using the fringe patterns obtained in X-ray reflectivity measurements, we confirmed that the films had an ~100-nm thickness (Fig. S2). To determine the oxidation states of vanadium, we carried out XPS (model ESCALAB 250Xi; Thermo Scientific) using a monochromatic Al source with a photon energy of 1486.6 eV under an environmental pressure of 10^{-8} Torr. To remove contamination, the film surface was sputtered with argon ions for 10 seconds[16]. We used the O 1s peak at 530.0 eV as the energy reference. We supplied electrons using an electron gun to avoid any charging effect.

References

1. Lee, S. *et al*. Electronic structure and insulating gap in epitaxial VO$_2$ polymorphs. *APL Mater.* **3**, 126109 (2015).
2. Lee, S., Ivanov, I. N., Keum, J. K. & Lee, H. N. Epitaxial stabilization and phase instability of VO$_2$ polymorphs. *Sci. Rep.* **6**, 19621 (2016).
3. Choi, S., Chang, S.-J., Oh, J., Jang, J. H. & Lee, S. Electrical and optical properties of VO$_2$ polymorphic films grown epitaxially on Y-stabilized ZrO$_2$. *Adv. Electron. Mater.* **4**, 1700620 (2018).
4. Driscoll, T. *et al*. Memory metamaterials. *Science* **325**, 1518 (2009).
5. Chang, S. H. *et al*. Oxide double-layer nanocrossbar for ultrahigh-density bipolar resistive memory. *Adv. Mater.* **23**, 4063 (2011).
6. Yang, Z., Ko, C. & Ramanathan, S. Oxide electronics utilizing ultrafast metal-insulator transitions. *Annu. Rev. Mater.* **41**, 337 (2011).
7. Lee, S. *et al*. Anomalously low electronic thermal conductivity in metallic vanadium dioxide. *Science* **355**, 371 (2017).
8. Lee, S. *et al*. Persistent electrochemical performance in epitaxial VO$_2$(B). *Nano Lett.* **17**, 2229 (2017).
9. Arcangeletti, E. *et al*. Evidence of a pressure-induced metallization process in monoclinic VO$_2$. *Phys. Rev. Lett.* **98**, 196406 (2007).
10. Wei, J., Ji, H., Guo, W., Nevidomskyy, A. H. & Natelson, D. Hydrogen stabilization of metallic vanadium dioxide in single-crystal nanobeams. *Nat. Nanotechnol.* **7**, 357 (2012).
11. Yoon, H. *et al*. Reversible phase modulation and hydrogen storage in multivalent VO$_2$ epitaxial thin films. *Nat. Mater.* **15**, 1113 (2016).
12. Nakano, M. *et al*. Collective bulk carrier delocalization driven by electrostatic surface charge accumulation. *Nature* **487**, 459 (2012).
13. Jeong, J. *et al*. Suppression of metal-insulator transition in VO$_2$ by electric field–induced oxygen vacancy formation. *Science* **339**, 1402 (2013).
14. Zylbersztejn, A. & Mott, N. F. Metal-insulator transition in vanadium dioxide. *Phys. Rev. B* **11**, 4383 (1975).
15. Shibuya, K., Kawasaki, M. & Tokura, Y. Metal-insulator transition in epitaxial V$_{1-x}$W$_x$O$_2$ ($0 \leq x \leq 0.33$) thin films. *Appl. Phys. Lett.* **96**, 022102 (2010).
16. Choi, S. *et al*. Sharp contrast in the electrical and optical properties of vanadium Wadsley (V$_m$O$_{2m}$ + 1, m > 1) epitaxial films selectively stabilized on (111)-oriented Y-stabilized ZrO$_2$. *Phys. Rev. Mater.* **3**, 063401 (2019).
17. Choi, S., Oh, J., Lee, J.-H., Jang, J. H. & Lee, S. Degradation mechanism of vanadium oxide films when grown on Y-stabilized ZrO2 above 500 °C. *Adv. Eng. Meter.* **21**, 1900918 (2019).
18. Choi, S. *et al*. High infrared transparency up to 8-μm-wavelength in correlated vanadium Wadsley conductors. *APL Mater.* **8**, 041111 (2020).
19. Shannon, R. D. Revised effective ionic radii and systematic studies of interatomic distances in halides and chalcogenides. *Acta. Cryst.* **A32**, 751 (1976).
20. Okuyama, D. *et al*. X-ray study of metal-insulator transitions induced by W doping and photoirradiation in VO$_2$ films. *Phys. Rev. B* **91**, 064101 (2015).
21. Ioffe, A. F. & Regel, A. R. Non-crystalline, amorphous and liquid electronic semiconductors. *Prog. Semicond.* **4**, 237 (1960).
22. Takami, H., Kanki, T., Ueda, S., Kobayashi, K. & Tanaka, H. Filling-controlled Mott transition in W-doped VO$_2$. *Phys. Rev. B* **85**, 205111 (2012).
23. Fox, M. *Optical properties of solids*. (Oxford University Press, Oxford, United Kingdom, 2010).

24. Lee, J. S., Shibuya, K., Kawasaki, M. & Tokura, Y. Optical investigation of metal-insulator transitions in $V_{1-x}W_xO_2$ ($0 \leq x \leq 0.33$). *Phys. Rev. B* **85**, 155110 (2012).
25. Booth, J. M. & Casey, P. S. Anisotropic structure deformation in the VO_2 metal-insulator transition. *Phys. Rev. Lett.* **103**, 086402 (2009).
26. Tan, X. *et al.* Unraveling metal-insulator transition mechanism of VO_2 triggered by tungsten doping. *Sci. Rep.* **2**, 466 (2012).
27. Sakai, E. *et al.* Competition between instabilities of Peierls transition and Mott transition in W-doped VO_2 thin films. *Phys. Rev. B* **84**, 195132 (2011).
28. Goodenough, J. B. The two components of the crystallographic transition in VO_2. *J. Solid State Chem.* **3**, 490 (1971).
29. Popuri, S. R. *et al.* VO_2(A): Reinvestigation of crystal structure, phase transition and crystal growth mechanisms. *J. Solid State Chem.* **213**, 79 (2014).
30. Takami, H., Kanki, T., Ueda, S., Kobayashi, K. & Tanaka, H. Electronic structure of W-doped VO_2 thin films with giant metal–insulator transition investigated by hard X-ray core-level photoemission spectroscopy. *Appl. Phys. Express* **3**, 063201 (2010).
31. Silversmit, G., Depla, D., Poelman, H., Marin, G. B. & De Gryse, R. Determination of the V 2p XPS binding energies for different vanadium oxidation states ($V5^+$ to $V0^+$). *J. Electron Spectrosc. Relat. Phenom.* **135**, 167 (2004).
32. Luo, X. *et al.* High carrier mobility in transparent $Ba_{1-x}La_xSnO_3$ crystals with a wide band gap. *Appl. Phys. Lett.* **100**, 172112 (2012).
33. Prakash, A. *et al.* Wide bandgap $BaSnO_3$ films with room temperature conductivity exceeding $10^4 \, S \, cm^{-1}$. *Nat. Commun.* **8**, 15167 (2017).
34. Lee, S., Meyer, T. L., Park, S., Egami, T. & Lee, H. N. Growth control of the oxidation state in vanadium oxide thin films. *Appl. Phys. Lett.* **105**, 223515 (2014).
35. Sze, S. M. & Ng, K. K. *Physics of semiconductor devices*. (Wiley, New York, United States, 2007).
36. Kuzmenko, A. B. Kramers–Kronig constrained variational analysis of optical spectra. *Rev. Sci. Instrum.* **76**, 083108 (2005).

Author contributions

S.C. conceived and performed the experiments under the supervision of S.L. S.C. and G.A. carried out spectroscopic ellipsometry and used a Fourier transform-type infrared spectrometer under the supervision of S.L. and S.J.M. S.C. and S.L. wrote the manuscript, and the other authors reviewed it.

Competing interests

The authors declare no competing interests.

Additional information

Supplementary information is available for this paper at https://doi.org/10.1038/s41598-020-66439-2.

Correspondence and requests for materials should be addressed to S.L.

Reprints and permissions information is available at www.nature.com/reprints.

Publisher's note Springer Nature remains neutral with regard to jurisdictional claims in published maps and institutional affiliations.